

Mechanical Spin Control of Nitrogen-Vacancy Centers in Diamond

E. R. MacQuarrie, T. A. Gosavi, N. R. Jungwirth, S. A. Bhawe, and G. D. Fuchs*

Cornell University, Ithaca, New York 14853, USA

(Received 4 July 2013; published 27 November 2013)

We demonstrate direct coupling between phonons and diamond nitrogen-vacancy (NV) center spins by driving spin transitions with mechanically generated harmonic strain at room temperature. The amplitude of the mechanically driven spin signal varies with the spatial periodicity of the stress standing wave within the diamond substrate, verifying that we drive NV center spins mechanically. These spin-phonon interactions could offer a route to quantum spin control of magnetically forbidden transitions, which would enhance NV-based quantum metrology, grant access to direct transitions between all of the spin-1 quantum states of the NV center, and provide a platform to study spin-phonon interactions at the level of a few interacting spins.

DOI: 10.1103/PhysRevLett.111.227602

PACS numbers: 76.30.Mi, 63.20.kp, 72.55.+s, 77.55.hd

As spin-based quantum technology evolves, the ability to manipulate spin with nonmagnetic fields could enable an interface for hybrid quantum systems and facilitate integration with conventional technology. Particularly useful examples are electric fields, optical fields, and mechanical lattice vibrations. The last of these represents direct spin-phonon coupling, which has garnered fundamental interest as a potential mediator of spin-spin interactions [1,2].

Nitrogen-vacancy (NV) center spins in diamond are a promising solid-state platform for quantum information science [3,4] and precision metrology. They are sensitive magnetometers [5,6], electrometers [7], and thermometers [8,9] with nanoscale spatial resolution due to their atomic size [10,11]. Significant progress in integrating NV centers with microelectromechanical systems (MEMS) has paved the way for studies of spins coupled to mechanical resonators [12–17]. In previous work, NV centers have been coupled to phonons indirectly, either by using a magnetic field gradient or by tuning the frequency of a magnetic spin transition. Here, we use a MEMS transducer to directly drive electronic spin transitions in NV centers using gigahertz-frequency mechanical (stress) waves. This work demonstrates direct spin-phonon interactions at room temperature as a means to drive magnetically forbidden spin transitions.

Driving spin transitions is the key to using NV center spins for quantum information science or sensing. Conventionally, quantum spin control in this system is accomplished with gigahertz-frequency magnetic fields [18–20] or with optical fields at cryogenic temperatures [21]. Resonant lattice vibrations couple to nuclear quadrupole moments [22] and represent another avenue to manipulate NV center electronic spins. NV centers couple to a magnetic field (B_{\parallel} and B_{\perp}) and a stress (σ_{\parallel} and σ_{\perp}) through their ground-state spin Hamiltonian [7,23]

$$H_{\text{NV}} = (D_0 + \epsilon_{\parallel}\sigma_{\parallel})S_z^2 + \gamma_{\text{NV}}B_{\parallel}S_z + \gamma_{\text{NV}}B_{\perp}S_x - \epsilon_{\perp}\sigma_x(S_x^2 - S_y^2) + \epsilon_{\perp}\sigma_y(S_xS_y + S_yS_x), \quad (1)$$

where $D_0 = 2.87$ GHz is the zero-field splitting, $\gamma_{\text{NV}} = 2.8$ MHz/G is the gyromagnetic ratio, $\epsilon_{\perp} = 0.03$ MHz/MPa [1,24] and ϵ_{\parallel} are the perpendicular and axial stress coupling constants, and S_x , S_y , S_z are the x , y , and z components of the spin-1 operator, respectively. The z axis is defined along the NV symmetry axis as depicted in Fig. 1(a).

In the S_z basis, H_{NV} has eigenstates $\{|(m_s=)0\rangle, | +1\rangle, | -1\rangle\}$. D_0 breaks the degeneracy between the $|0\rangle$ and $|\pm 1\rangle$ spin states at zero magnetic field. Careful alignment of a static external magnetic field B_{\parallel} along the NV

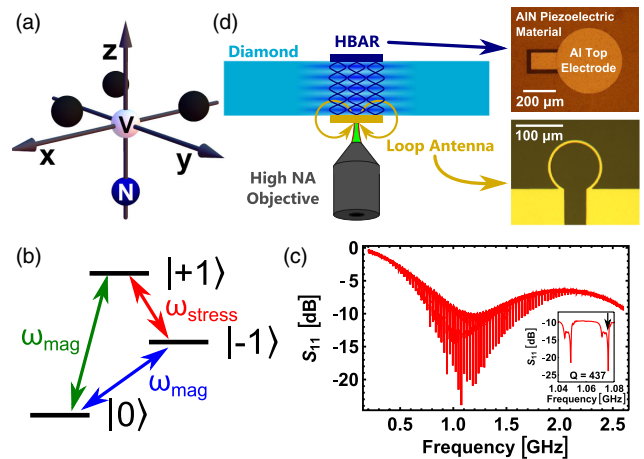


FIG. 1 (color online). (a) Schematic of an NV center. The z axis corresponds to the symmetry axis of the NV center. (b) Levels of an NV center ground-state spin. Magnetic driving enables $\Delta m_s = \pm 1$ transitions, whereas mechanical driving can produce $\Delta m_s = \pm 2$ transitions. (c) Reflected microwave power (S_{11}) as a function of frequency from the MEMS device measured using a network analyzer. Standing wave resonances have Q s as high as 437. (d) Device schematic. A loop antenna produces gigahertz-frequency magnetic fields for magnetic control while an HBAR produces gigahertz-frequency stress standing waves within the diamond.

symmetry axis zeros the static component of B_{\perp} and splits the $|+1\rangle$ and $|-1\rangle$ states. For conventional magnetic spin driving, an oscillating B_{\perp} can drive spin transitions from the $|0\rangle$ state to either the $|+1\rangle$ or the $|-1\rangle$ state. Similarly, a perpendicular stress couples the $|+1\rangle$ and $|-1\rangle$ states, allowing a direct $|+1\rangle \leftrightarrow |-1\rangle$ spin transition to be driven by a gigahertz-frequency stress wave resonant with the spin-state splitting. In the S_z basis, this transition is magnetically forbidden by the magnetic dipole selection rule, $\Delta m_s = \pm 1$. Thus, the ability to drive $|+1\rangle \leftrightarrow |-1\rangle$ with an oscillating stress wave and $|0\rangle \leftrightarrow |\pm 1\rangle$ with oscillating magnetic fields establishes direct transitions between all three spin levels, as depicted in Fig. 1(b). Additionally, an axial stress σ_{\parallel} shifts $|+1\rangle$ and $|-1\rangle$ equivalently and, therefore, has no effect on mechanical spin control performed in the $|\pm 1\rangle$ spin subspace.

The stress coupling coefficient ϵ_{\perp} is small enough that a large stress is required to produce a driving field comparable to those achieved with magnetic fields. To drive a large stress resonant with gigahertz-frequency spin transitions, we fabricated high-overtone bulk acoustic resonators (HBARs) [25] on one face of a $300 \mu\text{m}$ thick, $\langle 100 \rangle$ diamond [26]. The type IIa diamond used in these measurements is dense with native NV centers ($\approx 3 \times 10^{14} \text{ NV/cm}^3$), placing ≈ 230 NVs inside the confocal volume of our microscope. These NV centers are randomly oriented along one of the four $\langle 111 \rangle$ crystal axes within the diamond. By aligning the static magnetic field B_{\parallel} with one such axis, we isolate a single NV species from the four possible orientations, leaving ≈ 58 NVs that contribute to the signal in our experiments. Those NV centers that are not aligned with B_{\parallel} are not resonant with our control pulses so their fluorescence contributes a constant background to our measurements that is subtracted during data processing.

The HBAR consists of a $3 \mu\text{m}$ thick aluminum nitride (AlN) piezoelectric film sandwiched between two $400 \mu\text{m}$ diameter metal electrodes. Applying a gigahertz-frequency voltage across the AlN launches a longitudinal stress wave into the diamond. The diamond substrate acts as an acoustic Fabry-Pérot cavity, generating stress standing wave resonances with a pitch determined by the speed of sound in the diamond and the substrate thickness. By measuring the microwave power reflected from the device (S_{11}), we observed the resonant frequency comb of an HBAR [Fig. 1(c)]. From this data, we used the Q -circle method [27] to find that the unloaded quality factor (Q) of each resonance, which is as high as $Q = 437$ for $\omega_{\text{HBAR}} = 2\pi \times 1.076 \text{ GHz}$. Based on a one-dimensional oscillator model [28], this corresponds to a stress of $\sigma_{\text{max}} \approx 10 \text{ MPa}$ directed along the $[001]$ crystal axis of the diamond for 25 dBm of applied microwave power. By transforming the resulting stress tensor from the lattice coordinates to the coordinates of the NV center, we estimate the applied perpendicular stress to be $\sigma_{\perp} \approx 7 \text{ MPa}$ [26]. This is enough for an $\Omega_{\text{stress}} \approx 2\pi \times 210 \text{ kHz}$ spin driving field.

On the opposite face of the diamond, we fabricated a loop antenna for magnetic spin control [Fig. 1(d)].

To demonstrate mechanical spin control, we performed optically detected mechanical spin resonance (ODMSR) measurements of the $|-1\rangle \rightarrow |+1\rangle$ spin transition. The pulse sequences used for this experiment are shown in Fig. 2(a). First, the NV center ensemble is initialized into $|0\rangle$ by optical pumping with a 532 nm laser. The laser is then turned off and a magnetic adiabatic passage through the $|0\rangle \rightarrow |-1\rangle$ resonance robustly transfers the initialized spin population into the $|-1\rangle$ state [26,29]. The stress wave is then turned on for $6 \mu\text{s}$ at a frequency ω_{HBAR} corresponding to a resonance of the HBAR. Pulsing the stress wave ensures that any axial stress generated by the HBAR has no effect on the $|0\rangle \leftrightarrow |-1\rangle$ magnetic driving. After this stress pulse, a second magnetic adiabatic passage transfers the population remaining in $|-1\rangle$ to the $|0\rangle$ state. Fluorescence read out of the population in the $|0\rangle$ state is then performed, giving the signal for the experiment. Fluorescence read out is also performed after initialization into the $|0\rangle$ state to provide normalization for each iteration of the duty cycle. By repeating this sequence as a function of B_{\parallel} , we scan $\omega_{\pm 1}$, the energy splitting between $|+1\rangle$ and $|-1\rangle$. Whenever $\omega_{\pm 1} = \omega_{\text{HBAR}}$, the strain pulse transfers population from $|-1\rangle$ to $|+1\rangle$. Population transferred to $|+1\rangle$ during the stress pulse shows up as missing population in $|0\rangle$ via fluorescence measurement at the end of the duty cycle.

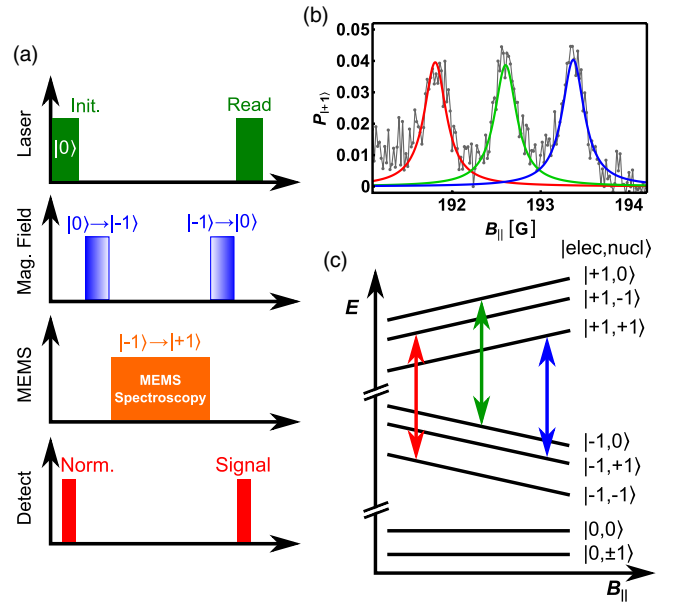


FIG. 2 (color online). (a) Pulse sequence used for ODMSR measurements. (b) Population driven into the $|+1\rangle$ state by the mechanical driving field as a function of the axial magnetic field B_{\parallel} for $\omega_{\text{HBAR}} = 2\pi \times 1.076 \text{ GHz}$ at room temperature. (c) NV hyperfine structure labeled with the experimentally observed transitions. Each arrow corresponds with the resonance condition $\omega_{\pm 1} = \omega_{\text{HBAR}}$ for each of the three nuclear spin sublevels.

Typical ODMSR results are shown in Fig. 2(b). The spectrum shows three peaks with 0.78 ± 0.02 G spacing. This corresponds to the $A/\gamma_{\text{NV}} = 0.77$ G hyperfine splitting arising from interactions between the NV spins and the unpolarized nuclear spins of the ^{14}N atoms neighboring the vacancies [23,26]. Because the nuclear spins are not polarized, only one third of the spins are resonant with each hyperfine sublevel, which reduces the contrast by a factor of 3. The contrast is also reduced by inhomogeneous mechanical driving of the NV ensemble. To account for dephasing and inhomogeneous driving, we calibrate the spin contrast by driving with conventional magnetic spin resonance [26]. For the resonance at $\omega_{\text{HBAR}} = 2\pi \times 1.076$ GHz, we estimate the peak mechanical driving field is $\Omega_{\text{stress}} \approx 2\pi \times 230$ kHz. This is consistent with the coupling strength of 0.03 MHz/MPa, which was previously determined from measurements of static strain at low temperature [1,24]. For scale, a single NV with a polarized nuclear spin driven at a stress antinode of this resonance would show 14% spin contrast. We also verified that the spin contrast scales with the mechanical Q by measuring ODMSR at an HBAR resonance with a different Q [26].

Because stress and electric fields enter the NV spin Hamiltonian in the same way [23], we verified that the ODMSR signals do not result from stray electric fields. To address this possibility, we used the finite element analysis software ANSYS HFSS to simulate the electric field generated during the stress pulse, which comprises the dominant source of stray electric fields in the experiment. The loop antenna on the rear face of the diamond was included. The simulated electric field within the relevant region of the diamond was no larger than $E_{\text{sim}} = 10$ V/cm. The coupling strength between a perpendicular electric field and the NV ground state spin is $d_{\text{gs}}^{\perp} = 17 \pm 3$ Hz cm/V [7,30]. Under conservative assumptions, E_{sim} would generate a driving field roughly 3 orders of magnitude lower than observed in the experiment. We also considered, but ruled out, magnetic driving of the $|+1\rangle \leftrightarrow |-1\rangle$ transition via stray magnetic fields from the MEMS transducer [26].

As a critical verification that we drive spin transitions with mechanically generated stress waves, we investigated how the ODMSR signal varies as a function of depth. Because we drive a stress standing wave, we expect that the ODMSR signal will be modulated at the periodicity of the standing wave. Taking care to account for optical aberrations introduced from refraction at the air-diamond interface [31], we repeated ODMSR measurements of the $\omega_{\text{HBAR}} = 2\pi \times 0.942$ GHz mechanical resonance at different depths within the sample. To correctly interpret the results, we note that our microscope collects fluorescence from all of the NV centers within its confocal volume. Figure 3(a) depicts schematically the variation in stress amplitude across an approximate confocal point spread function (PSF). Different regions within the confocal

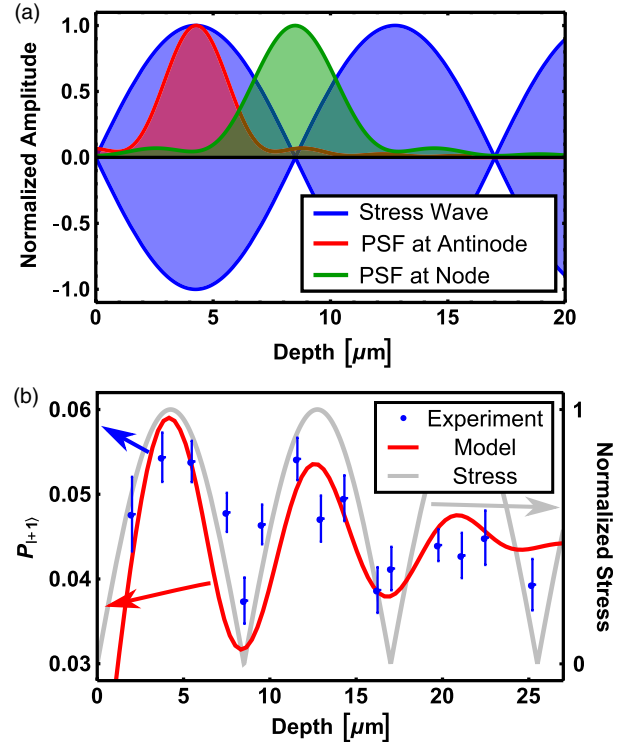


FIG. 3 (color online). (a) Normalized PSF of our confocal microscope plotted at a node and an antinode of the stress standing wave. (b) Peak ODMSR signal as a function of depth inside the diamond. The oscillations as a function of focal depth correspond to oscillations in stress along the standing wave used to drive spin transitions.

volume experience different stress driving fields, and we sample the range of stresses within the PSF. This reduces the spatial resolution in the focal direction and contributes to the inhomogeneous spin dephasing of the NV centers.

The ODMSR signal depends on the overlap between the oscillating stress and the PSF of the microscope, which is a maximum at an antinode of the stress standing wave. In contrast, ODMSR measured at a node is reduced by a factor of 1.5 [Fig. 3(b)]. Our approximate model, which is not a fit to the data, reproduces this ratio and the structure of the measured oscillation. To calculate the model curve, we convolve the stress standing wave with an approximated PSF that accounts for distortions in the position and shape of the PSF as a function of focal depth inside the diamond [26]. Crucially, we find excellent agreement between the spatial periodicity of the measured signal and the $17 \mu\text{m}$ wavelength of the HBAR-generated standing wave. This wavelength was calculated from the speed of sound in diamond (16 km/s) that we determined from the HBAR resonance pitch and the sample thickness. The decay of the measured oscillation at large depths is due to refractive aberration of the optical PSF, which increases linearly as a function of depth. Taken together, these observations are the “smoking gun” for mechanically driven spin transitions because the stress standing

wave is the only element of the experiment with spatial periodicity.

The modest ODMSR amplitudes of these measurements are limited by the amplitude of the stress wave, the power handling capabilities, and the driving field inhomogeneities in this first generation of devices. Because of these device limitations, we observe only incoherent driving of NV center spins. Improvements in device fabrication are estimated to increase the HBAR Q s by greater than a factor of 5 at room temperature [32], and cooling the samples to cryogenic temperature can increase the Q by a factor of $\approx 10^3$ [33]. Driving field inhomogeneities can be dispelled by driving either a single NV or a lateral plane of NVs, either of which would select a single value of the stress wave amplitude. Upon instituting these modest engineering improvements, we expect that coherent driving of the NV spin state is possible, putting stress driving on equal footing with magnetic driving.

Such control could have a number of practical sensing applications. Fang *et al.* demonstrated that using a $|\pm 1\rangle$ qubit for NV magnetometry enhances sensitivity and provides isolation from temperature fluctuations [6]. Because it directly couples the relevant states, mechanical driving could be useful for dynamical inversion of the $|\pm 1\rangle$ qubit, providing an alternative to $|\pm 1\rangle$ inversions constructed from a series of magnetic pulses that use $|0\rangle$ as a waypoint. Additionally, the spin signal from mechanically driven NV centers could be used as a precision sensor for gigahertz-frequency strains. One practical use may be to integrate NV centers with a MEMS accelerometer where acceleration shifts the intensity of ac strain. This would combine the high sensitivity of MEMS inertial sensing with the long-term stability of a spin transition, in a similar spirit to proposals for NV-based gyroscopes [34,35]. At low temperatures, it has been predicted that NV centers interacting with the cavity phonons of a mechanical resonator can generate a spin-squeezed state [1], and conversely, driven NV centers can be used to coherently cool or drive cavity phonons [17]. The mechanical spin driving presented here is the first step towards achieving these goals.

The development of new technology based on quantum spins in the solid state will depend on integration with both existing technology and other qubit systems. We have demonstrated spin manipulation through a direct interaction between spins and resonantly driven cavity phonons, thus, providing a new tool for integration and a new avenue for fundamental studies of spin-phonon interactions.

This work was supported by the Cornell Center for Materials Research with funding from the NSF MRSEC Program (No. DMR-1120296) and the Department of Energy Office of Science Graduate Fellowship Program (DOE SCGF), made possible in part by the American Recovery and Reinvestment Act of 2009, administered by ORISE-ORAU under Contract No. DE-AC05-06OR23100. Device fabrication was performed in part at

the Cornell NanoScale Science and Technology Facility, a member of the National Nanotechnology Infrastructure Network, which is supported by the National Science Foundation (Grant No. ECCS-0335765).

*gdf9@cornell.edu

- [1] S. D. Bennett, N. Y. Yao, J. Otterbach, P. Zoller, P. Rabl, and M. D. Lukin, *Phys. Rev. Lett.* **110**, 156402 (2013).
- [2] A. Albrecht, A. Retzke, F. Jelezko, and M. B. Plenio, *New J. Phys.* **15**, 083014 (2013).
- [3] H. Bernien, B. Hensen, W. Pfaff, G. Koolstra, M. S. Blok, L. Robledo, T. H. Taminiau, M. Markham, D. J. Twitchen, L. Childress, and R. Hanson, *Nature (London)* **497**, 86 (2013).
- [4] L. Childress, M. V. Gurudev Dutt, J. M. Taylor, A. S. Zibrov, F. Jelezko, J. Wrachtrup, P. R. Hemmer, and M. D. Lukin, *Science* **314**, 281 (2006).
- [5] P. Maletinsky, S. Hong, M. S. Grinolds, B. Hausmann, M. D. Lukin, R. L. Walsworth, M. Loncar, and A. Yacoby, *Nat. Nanotechnol.* **7**, 320 (2012).
- [6] K. Fang, V. M. Acosta, C. Santori, Z. Huang, K. M. Itoh, H. Watanabe, S. Shikata, and R. G. Beausoleil, *Phys. Rev. Lett.* **110**, 130802 (2013).
- [7] F. Dolde, H. Fedder, M. W. Doherty, T. Nöbauer, F. Rempp, G. Balasubramanian, T. Wolf, F. Reinhard, L. C. L. Hollenberg, F. Jelezko, and J. Wrachtrup, *Nat. Phys.* **7**, 459 (2011).
- [8] D. M. Toyli, C. F. de las Casas, D. J. Christle, V. V. Dobrovitski, and D. D. Awschalom, *Proc. Natl. Acad. Sci. U.S.A.* **110**, 8417 (2013).
- [9] G. Kucsko, P. C. Maurer, N. Y. Yao, M. Kubo, H. J. Noh, P. K. Lo, H. Park, and M. D. Lukin, *Nature (London)* **500**, 54 (2013).
- [10] H. J. Mamin, M. Kim, M. H. Sherwood, C. T. Rettner, K. Ohno, D. D. Awschalom, and D. Rugar, *Science* **339**, 557 (2013).
- [11] T. Staudacher, F. Shi, S. Pezzagna, J. Meijer, J. Du, C. A. Meriles, F. Reinhard, and J. Wrachtrup, *Science* **339**, 561 (2013).
- [12] P. Rabl, S. J. Kolkowitz, F. H. L. Koppens, J. G. E. Harris, and P. Z. M. D. Lukin, *Nat. Phys.* **6**, 602 (2010).
- [13] B. D'Urso, M. V. G. Dutt, S. Dhinra, and N. M. Nusran, *New J. Phys.* **13**, 045002 (2011).
- [14] S. Kolkowitz, A. C. Bleszynski Jayich, Q. P. Unterreithmeier, S. D. Bennett, P. Rabl, J. G. E. Harris, and M. D. Lukin, *Science* **335**, 1603 (2012).
- [15] S. Hong, M. S. Grinolds, P. Maletinsky, R. L. Walsworth, M. D. Lukin, and A. Yacoby, *Nano Lett.* **12**, 3920 (2012).
- [16] P. Ovartchaiyapong, L. M. A. Pascal, B. A. Myers, P. Lauria, and A. C. B. Jayich, *Appl. Phys. Lett.* **101**, 163505 (2012).
- [17] K. V. Keesidis, S. D. Bennett, S. Portolan, M. D. Lukin, and P. Rabl, *Phys. Rev. B* **88**, 064105 (2013).
- [18] V. V. Dobrovitski, G. D. Fuchs, A. L. Falk, C. Santori, and D. D. Awschalom, *Annu. Rev. Condens. Matter Phys.* **4**, 23 (2013).
- [19] F. Jelezko, T. Gaebel, I. Popa, A. Gruber, and J. Wrachtrup, *Phys. Rev. Lett.* **92**, 076401 (2004).

- [20] G.D. Fuchs, V.V. Dobrovitski, D.M. Toyli, F.J. Heremans, and D.D. Awschalom, *Science* **326**, 1520 (2009).
- [21] C.G. Yale, B.B. Buckley, D.J. Christle, G. Burkard, F.J. Heremans, L.C. Bassett, and D.D. Awschalom, *Proc. Natl. Acad. Sci. U.S.A.* **110**, 7595 (2013).
- [22] D.I. Bolef and R.K. Sundfors, *Nuclear Acoustic Resonance* (Academic, New York, 1993).
- [23] M.W. Doherty, F. Dolde, H. Fedder, F. Jelezko, J. Wrachtrup, N.B. Manson, and L.C.L. Hollenberg, *Phys. Rev. B* **85**, 205203 (2012).
- [24] E. Togan, Y. Chu, A.S. Trifonov, L. Jiang, J. Maze, L. Childress, M.V.G. Dutt, A.S.S. rensen, P.R. Hemmer, A.S. Zibrov, and M.D. Lukin, *Nature (London)* **466**, 730 (2010).
- [25] K.M. Lakin, G.R. Kline, and K.T. McCarron, *IEEE MTT-S Int. Microwave Symp. Dig.* **3**, 1517 (1993).
- [26] See Supplemental Material at <http://link.aps.org/supplemental/10.1103/PhysRevLett.111.227602> for additional experimental details and calculations.
- [27] D.A. Feld, R. Parker, R. Ruby, P. Bradley, and S. Dong, in *IEEE International Ultrasonics Symposium (IUS), Beijing, 2008* (IEEE, Piscataway, NJ, 2008), p. 431.
- [28] K.F. Graff, *Wave Motion in Elastic Solids* (Dover, New York, 1991).
- [29] C.P. Slichter, *Principles of Magnetic Resonance* (Springer, New York, 1990), 3rd ed.
- [30] E. Vanoort and M. Glasbeek, *Chem. Phys. Lett.* **168**, 529 (1990).
- [31] S. Hell, G. Reiner, C. Cremer, and E.H.K. Stelzer, *J. Microsc.* **169**, 391 (1993).
- [32] B.P. Sorokin, G.M. Kvashnin, A.P. Volkov, V.S. Bormashov, V.V. Aksenonkov, M.S. Kuznetsov, G.I. Gordeev, and A.V. Telichko, *Appl. Phys. Lett.* **102**, 113507 (2013).
- [33] T. Cheng, J. Hsiao, S.A. Bhave, and A. Duwel (to be published).
- [34] A. Ajoy and P. Cappellaro, *Phys. Rev. A* **86**, 062104 (2012).
- [35] M.P. Ledbetter, K. Jensen, R. Fischer, A. Jarmola, and D. Budker, *Phys. Rev. A* **86**, 052116 (2012).